

Simulating and exploring Weyl semimetal physics with cold atoms in a two-dimensional optical lattice

Dan-Wei Zhang,^{1,*} Shi-Liang Zhu,^{2,3,†} and Z. D. Wang^{1,‡}

¹*Department of Physics and Center of Theoretical and Computational Physics,
The University of Hong Kong, Pokfulam Road, Hong Kong, China*

²*National Laboratory of Solid State Microstructures and School of Physics, Nanjing University, Nanjing 210093, China*

³*Synergetic Innovation Center of Quantum Information and Quantum Physics,
University of Science and Technology of China, Hefei 230026, China*

(Dated: June 7, 2021)

We propose a scheme to simulate and explore Weyl semimetal physics with ultracold fermionic atoms in a two-dimensional square optical lattice subjected to experimentally realizable spin-orbit coupling and an artificial dimension from an external parameter space, which may increase experimental feasibility compared with the cases in three-dimensional optical lattices. It is shown that this system with a tight-binding model is able to describe essentially three-dimensional Weyl semimetals with tunable Weyl points. The relevant topological properties are also addressed by means of the Chern number and the gapless edge states. Furthermore, we illustrate that the mimicked Weyl points can be experimentally detected by measuring the atomic transfer fractions in a Bloch-Zener oscillation, and the characteristic topological invariant can be measured with the particle pumping approach.

PACS numbers: 37.10.Jk, 03.67.Ac, 03.65.Vf, 72.90.+y

I. INTRODUCTION

Weyl semimetal (WSM), as an exotic topologically nontrivial state of matter in three dimensions (3D) [1–8], has a singly-degenerate band structure with paired bulk band crossings, named as Weyl points. A linear dispersion relation in all three momentum directions exhibits near a Weyl point, with low-energy excitations resembling the well-known Weyl fermions in particle physics. Each Weyl point has a topological charge, namely the Chern number on the gapped 2D sphere enclosing a Weyl point in momentum space, and a pair of points with opposite charges support topologically protected gapless Fermi arc surface states [3–10]. The Weyl points and the Fermi arcs in a WSM are fundamentally interesting, and are expected to give rise to exotic phenomena absent in fully gapped topological phases, such as anomalous electromagnetic responses [8, 11, 12]. Recently, more and more efforts have been made on experimental realization of WSMs in real materials [13–17] and in artificial systems, such as analogous Weyl points in photonic crystals [18, 19].

On the other hand, ultracold atomic gases in optical lattices provide a powerful platform to simulate various quantum states of matter [20, 21]. In particular, recent experimental advances in engineering spin-orbit coupling and artificial gauge field for ultracold atoms [22–26] have pushed this system to the forefront for studying topological states of matter [27–41]. Another recently developed

technique related to the realization of topological phases in cold atom systems (also in photonic quasicrystals, e.g. see Ref. [42]) is extending an artificial dimension in optical lattices provided by an external cyclical parameter [43, 44] or the internal atomic degrees of freedom [45, 46]. Using this technique, one can study the physics of topological states in optical lattices attributed to dimensions higher than their own. Nowadays, the Zak phase in topologically nontrivial Bloch bands realized in 1D optical lattices has been measured [39]. The 2D Chern insulators and the Hofstadter bands have been also realized experimentally in 2D optical lattices with the Chern number therein being successfully probed [40, 41]. The experimental observation of chiral edge states in 1D optical lattices subjected a synthetic magnetic field and an artificial dimension has been reported [46]. By stacking multilayers of 2D atomic Chern or Hofstadter insulators, it was proposed to realize WSMs in 3D optical lattices [47–49]. This construction method was extended to simulate WSMs in 1D double-well optical lattices with two degrees of freedoms modulating the hopping terms [50], but it seems extremely hard to independently control them in practical experiments. Due to the elusive nature of WSMs and their intrinsic exotic properties, other feasible schemes for their experimental realization or simulation would be still of great value. In particular, the simulation and detection of the Weyl points and the relevant topological properties of WSMs with an artificial dimension in feasible 2D cold atomic systems are still badly awaited.

In this paper, we propose a scheme to simulate and explore essential physics of WSMs with ultracold fermionic atoms in a 2D square optical lattice, subjected to experimentally realizable spin-orbit coupling and an artificial dimension from an external cyclical parameter. We

*Electronic address: zdanwei@hku.hk

†Electronic address: slzhu@nju.edu.cn

‡Electronic address: zwang@hku.hk

first show that this system with a tight-binding model is able to mimic 3D WSMs with tunable Weyl points. The topological properties in this system are then further investigated by calculating the out-of-plane momentum, say k_z , -dependent Chern number and the gapless edge states. Finally, we propose practical methods for the experimental detection of the mimicked Weyl points and the characteristic topological invariant in the proposed cold atomic system. With numerical simulations, we demonstrate that the analogous Weyl points in this system can be sharply probed by measuring the Landau-Zener tunneling to the excited band after a Bloch oscillation and the k_z -dependent Chern number can directly be extracted from the center shift of the hybrid Wannier functions, both of which are measurable with cold atoms in optical lattices by the time-of-flight images. Comparing with the schemes evolving complex synthetic magnetic fluxes in 3D optical lattices [47–49], our scenario not only is different but also may increase experimental feasibility. In addition, the proposed system with high tunability and convenient detection ways may provide a promising platform for exploring exotic WSM physics.

The paper is organized as follows. Section II introduces the cold atom system with a tight-binding model for simulating the WSM phase with tunable Weyl points. In Sec. III, we elaborate the topological properties in this model by calculating the k_z -dependent Chern number and gapless edge states. In section IV, we propose practical methods for the experimental detection of the mimicked Weyl points and the characteristic topological invariant in the proposed cold atomic system with numerical simulations. Finally, a short conclusion is given in Sec. V.

II. MODEL

In this section, we construct a tight-binding model in a 2D square lattice subjected to an artificial dimension for simulating the tunable WSM phase. Let us consider a non-interacting spin-1/2 ultracold degenerate fermionic gas (labeled as spins \uparrow and \downarrow) loaded in a 2D square optical lattice in the xz plane. In the tight-binding regime, the atomic hopping between two nearest-neighbor lattice sites can be spin-conserved hopping or spin-flip hopping which can be achieved by Raman coupling between the two spin states $|\uparrow\rangle$ and $|\downarrow\rangle$ [26]. The tight-binding Hamiltonian of this cold atom system is considered to be

$$\hat{\mathcal{H}} = \hat{H}_L + \hat{H}_{SOC} + \hat{H}_P, \quad (1)$$

which consists of the spin-conserved hopping in the 2D lattice \hat{H}_L , the spin-flip hopping along the x axis \hat{H}_{SOC} , and \hat{H}_P representing additional external coupling poten-

tial:

$$\hat{H}_L = - \sum_{\mathbf{i}, \sigma, \eta} t_\sigma \left(\hat{a}_{\mathbf{i}, \sigma}^\dagger \hat{a}_{\mathbf{i} + \hat{\eta}, \sigma} + \text{h.c.} \right), \quad (2)$$

$$\hat{H}_{SOC} = -t_s \sum_{\mathbf{i}} \left(\hat{a}_{\mathbf{i}, \uparrow}^\dagger \hat{a}_{\mathbf{i} + \hat{x}, \downarrow} - \hat{a}_{\mathbf{i}, \downarrow}^\dagger \hat{a}_{\mathbf{i} - \hat{x}, \downarrow} + \text{h.c.} \right), \quad (3)$$

$$\begin{aligned} \hat{H}_P = & \Gamma_z \sum_{\mathbf{i}} \left(\hat{a}_{\mathbf{i}, \uparrow}^\dagger \hat{a}_{\mathbf{i}, \uparrow} - \hat{a}_{\mathbf{i}, \downarrow}^\dagger \hat{a}_{\mathbf{i}, \downarrow} \right) \\ & + \Gamma_x \sum_{\mathbf{i}} \left(\hat{a}_{\mathbf{i}, \uparrow}^\dagger \hat{a}_{\mathbf{i}, \downarrow} + \hat{a}_{\mathbf{i}, \downarrow}^\dagger \hat{a}_{\mathbf{i}, \uparrow} \right). \end{aligned} \quad (4)$$

Here $\hat{a}_{\mathbf{i}, \sigma}$ ($\hat{a}_{\mathbf{i}, \sigma}^\dagger$) annihilates (creates) a fermion on site $\mathbf{i} = (i_x, i_z)$ with spin $\sigma = \{\uparrow, \downarrow\}$ and $\eta = \{x, z\}$. The spin-dependent hopping amplitude t_σ in \hat{H}_L is assumed to be $t_\uparrow = -t_\downarrow = t_0$, which can be achieved in experiments by Raman laser or modulation engineering hopping [26], such as laser-induced Peierls phase factor $e^{i\pi}$ for the $|\downarrow\rangle$ atomic hopping. The spin-flip hopping term \hat{H}_{SOC} can be induced by the experimentally realized spin-orbit coupling with equal Rashba and Dresselhaus amplitudes through a two-photon Raman process [23–26]. Finally, the Hamiltonian \hat{H}_P is composed of a Zeeman potential and an additional coupling term on the spin states. The Zeeman potential is generated by an external magnetic field and the coupling term is induced by additional Raman lasers [51]. The Zeeman and Raman terms can be turned fully and independently in cold atom experiments with long coherence time [51], and thus we choose the parameters in the following forms

$$\Gamma_z = m_z - 2t_0 \cos \theta, \quad \Gamma_x = 2t_s \sin \theta, \quad (5)$$

where m_z is a constant parameter and θ is a cyclical parameter that can vary from $\theta = -\pi$ to $\theta = \pi$.

Under the period boundary condition, the total Hamiltonian of the system can be rewritten as

$$\hat{\mathcal{H}} = \sum_{\mathbf{k}, \sigma, \sigma'} \hat{a}_{\mathbf{k}\sigma}^\dagger [H(\mathbf{k})]_{\sigma\sigma'} \hat{a}_{\mathbf{k}\sigma'}, \quad (6)$$

where $\hat{a}_{\mathbf{k}\sigma} = 1/\sqrt{V} \sum_{\mathbf{i}} e^{-i\mathbf{k}\cdot\mathbf{i}} \hat{a}_{\mathbf{i}, \sigma}$ is the annihilation operators in momentum space $\mathbf{k} = (k_x, k_z)$, and $H(\mathbf{k})$ is the Bloch Hamiltonian given by $H(\mathbf{k}) = \vec{d}(\mathbf{k}) \cdot \vec{\sigma}$. Here $\vec{\sigma} = (\sigma_x, \sigma_y, \sigma_z)$ are the Pauli matrices acting on the atomic components and $\vec{d} = (d_x, d_y, d_z)$ is the Bloch vectors: $d_x = 2t_s \sin \theta$, $d_y = 2t_s \sin k_x$, and $d_z = m_z - 2t_0 \cos k_z - 2t_0 \cos k_x - 2t_0 \cos \theta$, with lattice spacing $a \equiv 1$ and $\hbar \equiv 1$ hereafter. The energy spectrum of the system is then given by $E_{\pm}(\mathbf{k}, \theta) = \pm |\vec{d}(\mathbf{k}, \theta)|$. Treating the cyclical parameter θ as the Bloch momentum k_y , which acts as an artificial dimension of the y axis under periodical condition along this direction, we can consider the 2D system in a 3D parameter space with the 3D-extended momentum $\tilde{\mathbf{k}} = (k_x, \theta, k_z)$. The bulk energy bands are fully gapped except the points that satisfy the following conditions:

$$\sin k_x = \sin \theta = 0, \quad (7)$$

$$m_z - 2t_0(\cos k_z + \cos k_x + \cos \theta) = 0, \quad (8)$$

which determine the boundaries between the mimicked WSM phase and the bulk insulating phases as discussed in the following.

We now show that the WSM phase can be simulated in this system. Without loss of generality, we focus on the parameters $t_0 > 0$, $t_s > 0$ and $m_z \geq 0$ in the system in the rest of this paper. The first condition of Eq. (7) requires $k_x = \{0, \pi\}$ and $\theta = \{0, \pi\}$, and consequently the second condition of Eq. (8) reduces to:

$$m_z - 2t_0 \cos k_z = 0, \text{ for } (k_x, \theta) = (0, \pi) \text{ and } (\pi, 0); \quad (9)$$

$$m_z - 2t_0 \cos k_z - 4t_0 = 0, \text{ for } (k_x, \theta) = (0, 0); \quad (10)$$

$$m_z - 2t_0 \cos k_z + 4t_0 = 0, \text{ for } (k_x, \theta) = (\pi, \pi). \quad (11)$$

When one of the three equations (9-11) is fulfilled with the double-valued $k_z \in [-\pi, \pi]$, a pair of degenerate points will exhibit in extended 3D band structure, which can be regarded as analogous Weyl points in the $\tilde{\mathbf{k}}$ space. For the considered parameter regime, Eq. (11) can not be fulfilled, while Eq. (9) gives rise to two pairs of analogous Weyl points denoted by $\mathbf{W}_{1,\pm} = (0, \pi, \pm \arccos \frac{m_z}{2t_0})$ and $\mathbf{W}_{2,\pm} = (\pi, 0, \pm \arccos \frac{m_z}{2t_0})$ for $m_z \leq 2t_0$. Eq. (10) gives rise to a single pair of Weyl points $\mathbf{W}_{\pm} = (0, 0, \pm \arccos \frac{m_z - 4t_0}{2t_0})$ for $2t_0 \leq m_z \leq 6t_0$. In Fig. 1, we plot the extended 3D bulk band structure $E_+(k_x, \theta, k_z)$ for the typical parameters m_z with fixed hopping energy $t_0 = t_s = 1$. Therefore, the mimicked Weyl points can be found in the positions where $E_+ = 0$. When $m_z = 1$ [Fig. 1(a)], two pairs of analogous Weyl points locate at $(k_x, \theta, k_z) = (0, \pi, \pm\pi/3)$ and $(\pi, 0, \pm\pi/3)$ as expected, and the critical case appears when $m_z = 2$ [Fig. 1(b)], with the two pairs merging at $(0, \pi, 0)$ and $(\pi, 0, 0)$, and another pair being created at $(0, 0, \pm\pi)$. When $m_z = 4$ [Fig. 1(c)], the newly created pair of analogous Weyl points move to the position $(0, 0, \pm\pi/2)$, and then merge at the location $(0, 0, 0)$ when increasing the parameter to the critical value $m_z = 6$. From Fig. 1, we can find that the number and location of the analogous Weyl points are able to be tuned just by varying the parameter m_z . This demonstrates that one can conveniently create, move, and merge the mimicked Weyl points in this cold atom system.

Without loss of generality, hereafter we focus on the simplest case of a single pair of Weyl points \mathbf{W}_{\pm} , where the bulk bands only touch at the two distinct points in the $\tilde{\mathbf{k}}$ space. We can expand the Bloch Hamiltonian around the two mimicked Weyl points up to linear order in $\tilde{\mathbf{k}}$, and then obtain the low-energy effective Hamiltonian

$$H_{W,\pm} = v_x q_x \sigma_y + v_y q_y \sigma_x \pm v_z q_z \sigma_z, \quad (12)$$

where $v_x = v_y = 2t_s$ and $v_z = 2t_0$ are the effective Fermi velocity, and $\mathbf{q} \equiv (q_x, q_y, q_z) = \tilde{\mathbf{k}} - \mathbf{W}_{\pm}$ for the two points, respectively. The Hamiltonian (12) is an analogous anisotropic Weyl Hamiltonian for the Weyl fermions and can be written as $H_{W,\pm} = \sum_{i,j} q_i \alpha_{ij} \sigma_j$, where $[\alpha_{ij}]$ is a 3×3 matrix with elements $\alpha_{xy} = \alpha_{yx} = 2t_s$, $\alpha_{zz} = \pm 2t_0$ and zero otherwise. Thus the chirality of the two Weyl

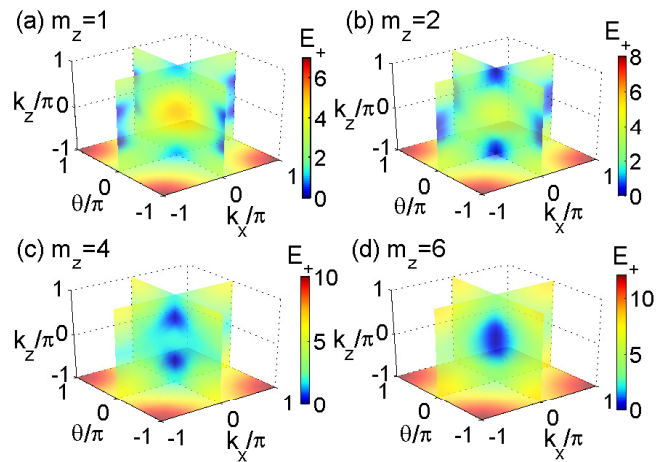


FIG. 1: (Color online) Color-coded extended 3D bulk band structure $E_+(k_x, \theta, k_z)$ for the typical parameters m_z . (a) $m_z = 1$ with two pairs of analogous Weyl points located at $(k_x, \theta, k_z) = (0, \pi, \pm\pi/3)$ and $(\pi, 0, \pm\pi/3)$; (b) $m_z = 2$, critical case with two pairs of analogous Weyl points merging at $(0, \pi, 0)$ and $(\pi, 0, 0)$, and another pair appear at $(0, 0, \pm\pi)$; (c) $m_z = 4$ with one pair of analogous Weyl points located at $(0, 0, \pm\pi/2)$; and (d) $m_z = 6$, critical case with the pair of analogous Weyl points merging at $(0, 0, 0)$. Other parameters in (a-d) are $t_0 = 1$ as the energy unit and $t_s = 1$.

points \mathbf{W}_{\pm} can be defined as $\chi_{\pm} = \text{sign}(\det[\alpha_{ij}]) = \pm 1$, respectively.

III. TOPOLOGICAL PROPERTIES

The opposite chirality of the paired analogous Weyl points reflects the topological properties of this system, which can be characterized by the corresponding topological charge. Actually, a mimicked Weyl point here can be regarded as a monopole in the $\tilde{\mathbf{k}}$ space, whose topological charge equals its chirality [9, 10]. The paired Weyl points are robust to perturbations which add a $\sigma_{x,y,z}$ term to the Hamiltonian because their charge is quantized: the monopole charge cannot vary under a continuous change of the Hamiltonian and they can only change at creation or annihilation of a monopole-antimonopole pair. Moreover, it was shown recently that the gapless edge modes of a WSM are also robust against disorders [8].

To further look into the topological properties of this system, we consider the Hamiltonian (1) with the so-called dimension reduction method. We treat k_z as an effective parameter and reduce the original system to a (k_z -modified) collection of effective 2D systems, as tight-binding chains along the x axis. Such a reduction method is valid for the bulk system and the reduced chains if k_z is a good quantum number. For a fixed quantum number, the reduced Bloch Hamiltonian $H(k_x, \theta, k_z) \rightarrow H_{k_z}(k_x, \theta)$, with

$$H_{k_z}(k_x, \theta) = 2t_s \sin \theta \sigma_x + 2t_s \sin k_x \sigma_y + (M_z - 2t_0 \cos k_x - 2t_0 \cos \theta) \sigma_z \quad (13)$$

acting as an effective 2D band structure in the $k_x - \theta$ parameter space, where $M_z = m_z - 2t_0 \cos k_z$. Since the extended 3D bulk bands are fully gapped when $k_z \neq \pm k_z^c$ with $k_z^c = \arccos[(m_z - 4t_0)/2t_0]$, in this case, $H_{k_z}(k_x, \theta)$ describes a system of the effective 2D Chern insulator. Therefore, one can have a well-defined Chern number

$$\begin{aligned} C_{k_z} &= \frac{1}{4\pi} \int_{-\pi}^{\pi} dk_x \int_{-\pi}^{\pi} d\theta \hat{d} \cdot (\partial_{k_x} \hat{d} \times \partial_{\theta} \hat{d}) \\ &= \begin{cases} -\text{sign}(M_z), & 0 < |M_z| < 4t_0; \\ 0, & |M_z| > 4t_0. \end{cases} \end{aligned} \quad (14)$$

where $\hat{d} \equiv \vec{d}/|\vec{d}|$. For our case within the parameter regime $2t_0 \leq m_z \leq 6t_0$, we can obtain that $C_{k_z} = -1$ when $k_z \in (-k_z^c, k_z^c)$ and otherwise $C_{k_z} = 0$. For each k_z -fixed chain with a nonzero Chern number, according to the bulk-edge correspondence and the index theorem [52], there must be topologically protected gapless if an edge is created, i.e. finite lattice sites along the x axis. This reduced system of 2D analogous Chern insulator is described by the reduced Bloch Hamiltonian $H_{k_z}(k_x, \theta)$, and the corresponding tight-binding chain Hamiltonian is given by

$$\begin{aligned} \hat{H}_C &= - \sum_{i_x} t_0 \left(\hat{a}_{i_x+1, \uparrow}^{\dagger} \hat{a}_{i_x, \uparrow} - \hat{a}_{i_x+1, \downarrow}^{\dagger} \hat{a}_{i_x, \downarrow} \right) + \text{h.c.} \\ &\quad - \sum_{i_x} t_s \left(\hat{a}_{i_x, \uparrow}^{\dagger} \hat{a}_{i_x+1, \downarrow} - \hat{a}_{i_x, \downarrow}^{\dagger} \hat{a}_{i_x-1, \downarrow} \right) + \text{h.c.} \\ &\quad + \sum_{i_x} (M_z - 2t_0 \cos \theta) \left(\hat{a}_{i_x, \uparrow}^{\dagger} \hat{a}_{i_x, \uparrow} - \hat{a}_{i_x, \downarrow}^{\dagger} \hat{a}_{i_x, \downarrow} \right) \\ &\quad + \sum_{i_x} 2t_s \sin \theta \left(\hat{a}_{i_x, \uparrow}^{\dagger} \hat{a}_{i_x, \downarrow} + \hat{a}_{i_x, \downarrow}^{\dagger} \hat{a}_{i_x, \uparrow} \right). \end{aligned} \quad (15)$$

In Fig. 2, we numerically calculate the energy spectrum of the reduced chain with length $L_x = 40$ under open boundary conditions for different parameters. From Figs. 2(a-c), we can see the variation of the energy spectrum by changing the parameter k_z for fixed $m_z = 4t_0$. For $k_z = 0$ in Fig. 2(a), the spectrum contains two symmetric bands with an energy gap opened, which accompanies some in-gap modes splitting into two branches. The two branches of edge modes cross and connect the separated bands. It indicates that the system with the lower band filled is a topologically nontrivial insulator with Chern number $C_{k_z} = -1$. As we continuously increase the parameter k_z , the band gap closes at the critical value $k_z = k_z^c = 0.5\pi$ [Fig. 2(b)] and then reopens without the in-gap edge modes [Fig. 2(c)], indicating the system in the topologically trivial case with Chern number $C_{k_z} = 0$. Such a k_z -parameter induced transition between topologically distinct regimes in numerical simulations is consistent with the previous analytical calculations. In Figs. 2(d) and 2(e), we show the spectrum of topologically nontrivial states for $k_z = 0$ and $k_z = 0.5\pi$ with fixed $m_z = 3t_0$, in which cases the critical value is $k_z^c = 2\pi/3$. Despite the shapes of the spectra being somewhat different, the existence of continuous edge

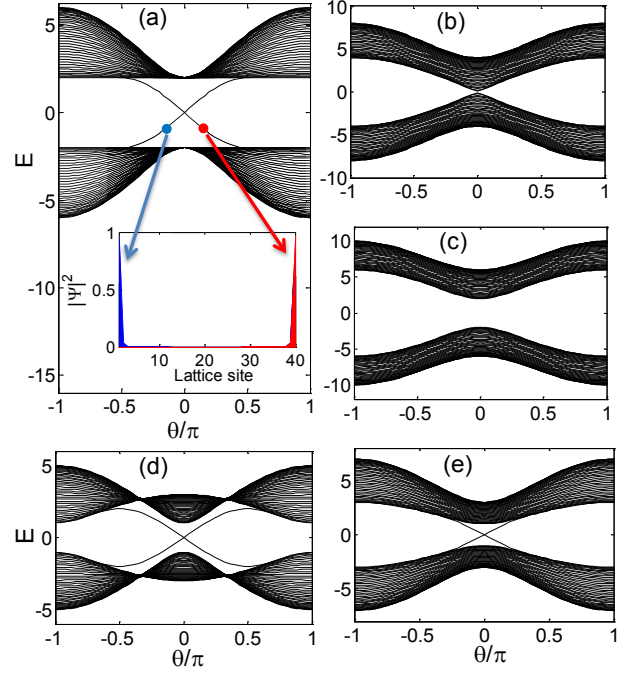


FIG. 2: (Color online) Energy spectrum of the reduced tight-binding chain of analogous Chern insulator with lattice sites $L_x = 40$ under open boundary conditions. (a) non-trivial case for $k_z = 0$ and $m_z = 4$; (b) critical case for $k_z = 0.5\pi$ and $m_z = 4$; (c) trivial case for $k_z = \pi$ and $m_z = 4$; (d) non-trivial case for $k_z = 0$ and $m_z = 3$; (e) non-trivial case for $k_z = 0.5\pi$ and $m_z = 3$. The insert figure in (a) shows the density distribution of two typical edge modes. Other parameters in (a-e) are $t_0 = 1$ as the energy unit and $t_s = 1$.

modes connecting the lower and upper bands indicates that the system is topologically nontrivial in these cases. The density distribution (profile) of the edge modes in these topologically nontrivial cases are similar to the two typical ones shown in the insert figure in Fig. 2(a), and they will gradually spread into the bulk when their energies are closer to the bulk bands.

In the context of 3D WSM phase, a pair of Weyl points can be viewed as a monopole-antimonopole pair in the momentum space. As a consequence of these monopoles, there are chiral Fermi surfaces with the energy $E = 0$ connecting the Weyl points on the surface not perpendicular to the z axis, named as Fermi arc [3-8]. In this 2D system with an artificial dimension, in a similar way by assuming that θ and k_z are good quantum numbers, we can consider edge modes along the x axis in the mimicked WSM phase. The system in this case returns to the reduced chain described by Hamiltonian (15) and we find that analogous Fermi-arc zero modes emerge by numerically calculating the energy spectrum of the edge modes, as shown in Fig. 3. In this case, the pair of the analogous Weyl points are connected with straight Fermi lines consisting of gapless zero-energy edge modes, which are analogous to Fermi arcs in the $\theta - k_z$ parameter space (denote by green dashed lines). The correspond-

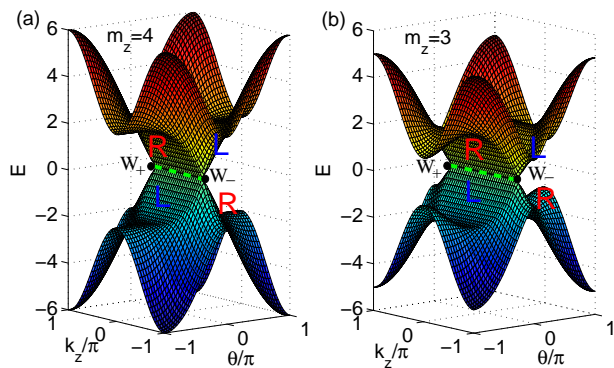


FIG. 3: (Color online) Energy spectrum of the edge states in the mimicked WSM phase for (a) $m_z = 4$ and (b) $m_z = 3$. The green dashed lines denote straight Fermi lines formed by gapless zero-energy edge modes, which are analogous to Fermi arcs connecting the pair of the mimicked Weyl points \mathbf{W}_\pm . They are located at $(\theta, k_z) = (0, \pm\pi/2)$ in (a) and $(\theta, k_z) = (0, \pm 2\pi/3)$ in (b), respectively. The regimes of left-edge and right-edge modes in the parameter space denoted by blue 'L' and red 'R' are $\{E < 0, \theta < 0\} \cup \{E > 0, \theta > 0\}$ and $\{E > 0, \theta < 0\} \cup \{E < 0, \theta > 0\}$, respectively. The edge modes have similar profiles with those shown in Fig. 2(a). Other parameters in (a) and (b) are $t_0 = 1$ as the energy unit and $t_s = 1$.

ing regimes for left-edge and right-edge modes are also shown in Fig. 3(a) and 3(b). The profiles of these edge modes are similar with those shown in Fig. 2(a), and the edge modes closer to the Weyl points and the bulk bands spread more into the bulk than those in the center of the parameter regime.

IV. EXPERIMENTAL DETECTION OF MIMICKED WSM PHASE

So far, we have introduced the system for simulating the WSM physics and explored the relevant topological properties. In this section, we propose practical methods for their experimental detection in this cold atom system. We first show that the mimicked Weyl points can be probed by measuring the atomic Zener tunneling to the excited band after a Bloch oscillation, and then propose a feasible technique to obtain the k_z -dependent Chern number directly from the center shift of the hybrid Wannier functions.

A. Detection of the Weyl points

The band touching points can be monitored from the atomic fraction tunnelling to the excited band in Bloch oscillations, as recently experimentally demonstrated to probe the Dirac points and the topological phase transition in a honeycomb optical lattice [53, 54]. This Bloch-Zener-oscillation technique can be extended to detect the

simulated Weyl points in 3D optical lattices [49] and in our system. Let us consider a 2D cloud of noninteracting fermions prepared in the ground band in this system and an external constant force F is applied along the η ($\eta = x, z$) direction, which pushes the atoms moving along the k_η direction. For fixed parameters θ and m_z , one can observe the quasi-momentum distribution of the transfer fraction in the excited band from the time-of-flight measurements after a Bloch cycle [53, 54]. One can perform such a measurement for varying parameters, and finally the mimicked Weyl points in the extended 3D Brillouin zone can be verified.

Without loss of generality, here we consider the case of a single pair of Weyl points described by the low-energy effective Hamiltonian (12). In this case, the transfer fraction $\xi_x(k_z)$ [$\xi_z(k_x)$] along the k_x (k_z) direction for k_z -trajectory (k_x -trajectory) can be written as [53, 54]

$$\xi_x(k_z) = P_{LZ}^x(k_z), \quad (16)$$

$$\xi_z(k_x) = 2P_{LZ}^z(k_x) \left[1 - P_{LZ}^z(k_x) \right], \quad (17)$$

where $P_{LZ}^x = e^{-\pi \Delta_x^2(k_z)/4v_x F}$ and $P_{LZ}^z = e^{-\pi \Delta_z^2(k_x)/4v_z F}$ are the Landau-Zener transition probabilities, with $\Delta_x = 2E_+(k_x = 0, k_z)$ and $\Delta_z = 2E_+(k_x, k_z = k_z^c)$ denoting the energy gaps for the Landau-Zener events along the k_η direction. For simplicity, here we treat trajectories for different k_η as independent by neglecting the harmonic trap and assuming the two tunneling events along the k_z direction incoherent. Such a simplified model was shown to be sufficient for comparison with the experiments under realistic conditions [53, 54].

In Fig. 4, we calculate the transfer fractions $\xi_{x,z}$ using Eqs. (16) and (17) for some typical parameters. The quasi-momentum distributions $\xi_x(k_z)$ for varying parameter θ in Figs. 4(a) (with $m_z = 3$) and 4(b) (with $m_z = 4$) show two maximum transfer positions in the whole $k_z - \theta$ space, which correspond to the k_z and θ positions of the paired Weyl points as expected. These peaks of the maximum transfer fractions are sharp since the transition probability in a single Landau-Zener event increases exponentially as the energy gap decreases. In other words, the emergence of the mimicked Weyl points, at which the band gap closes, is accompanied by a dramatic increase in the transfer fraction $\xi_x(k_z, \theta)$. In contrast, there are two subsequent Landau-Zener transitions along the k_z direction. This results in the distribution of the final transfer $\xi_z(k_x, \theta)$ exhibiting the ring-type profile of the maximum value $\xi_z = 0.5$, as shown in Figs. 4(c) and 4(d). The position of maximum dip with the value $\xi_z \approx 0$ inside the ring profile of $\xi_z(k_x, \theta)$ indicates $k_x = \theta = 0$ for the mimicked Weyl points in these cases. We also plot the distribution $\xi_x(k_z, m_z)$ for fixed $\theta = 0$ in Fig. 4(e), where the maximum transfer positions of $\xi_x(k_z)$ correspond well to the expected k_z positions of the mimicked Weyl points as plotted by the dashed line. The $\xi_x(k_z, \theta)$ distributions for different t_s will be modified, but the peaks of the transfer fractions remains, with an example shown in Fig. 4(f). Therefore, combining with

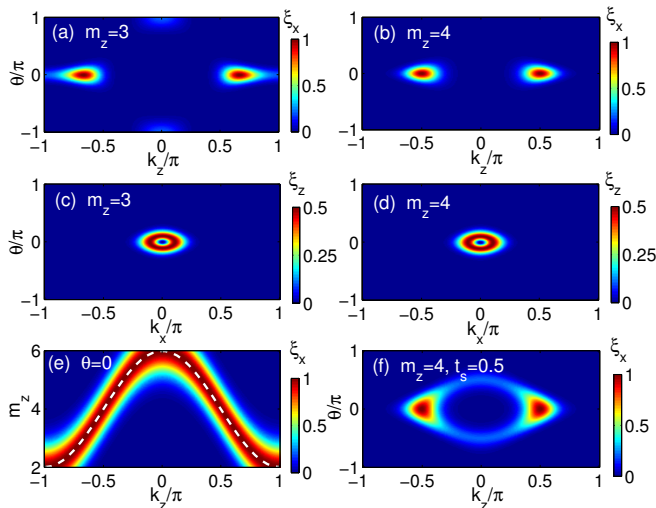


FIG. 4: (Color online) The transfer fractions for tunable parameters. The quasi-momentum distribution $\xi_x(k_z)$ for varying parameter θ with (a) $m_z = 3$ and (b) $m_z = 4$; the quasi-momentum distribution $\xi_z(k_x)$ for varying parameter θ with (c) $m_z = 3$ and (d) $m_z = 4$; (e) $\xi_x(k_z)$ for different parameter m_z with $\theta = 0$; (f) $\xi_x(k_z)$ for different parameter θ with m_z and $t_s = 0.5$. The white dashed line in (e) shows the expected k_z positions of the mimicked Weyl points \mathbf{W}_{\pm} for varying m_z , which are well agree with the maximum transfer positions of $\xi_x(k_z)$. The maximum $\xi_x(k_z, \theta)$ in (a) and (b) also correspond to the k_z and θ positions, as shown in Fig. 3. The position of maximum dip inside the ring profile of $\xi_z(k_x, \theta)$ in (c) and (d) indicates $k_x = \theta = 0$ for the Weyl points. Other parameters in (a-f) are $t_0 = 1$ as the energy unit, $F = 1$, and $t_s = 1$ except that $t_s = 0.5$ in (f).

the measurements of transfer distributions $\xi_x(k_z, \theta)$ and $\xi_z(k_x, \theta)$ from Bolch-Zener transitions along the k_x and k_z direction, one can resolve the mimicked Weyl points in the \mathbf{k} space for different m_z . This detection method is robust against fluctuations of the hopping strengths, which are engineered by laser beams in this cold atom system. In addition, since the creation or annihilation of the analogous Weyl points by external parameters (such as m_z) will accompany topological phase transition, then the critical point of the transition can be identified by using this method.

B. Detection of the k_z -dependent Chern number

In solid-state materials, the Chern number value can be revealed from a routine measurement of the Hall conductance, however, the detection method is usually quite different in cold atom systems [30, 33–36, 39–41, 55]. Since the Chern number comes from the integral of Berry curvature over the first Brillouin zone, one way to reveal the topological order is to measure the Berry curvature. It was theoretically proposed and experimentally performed in optical lattices to map the Berry curvature from the transverse drift induced by the anomalous ve-

locity in Bloch oscillations [33, 34, 40, 41] and from an atomic interferometry in momentum space [35, 39, 55]. Besides, it was also proposed to measure the Berry curvature from atomic momentum distributions for different spin and spin-mixing components [30, 36]. These methods for measuring the Berry curvature could be potentially extended to our proposed cold atom system, as one can perform similar measurements for a fixed value of the parameter θ .

Below we propose a practical method to directly probe the k_z -dependent Chern number given by Eq. (14) in our system, based on a generalization of topological pumping in optical lattices [56–58]. Remind that in order to obtain the topological invariant, we treat our 2D system as a collection of tight-binding chains along the x axis described by Hamiltonian (15), which can realize the analogous Chern insulators defined in the $k_x - \theta$ space as different slices of parameter k_z . The polarization of this 1D insulator can be expressed by means of the centers of the hybrid Wannier functions (HWFs) [59], which are localized in the x axis retaining Bloch character in the θ artificial dimension in our case. This polarization depends on the parameter k_z and is a function of θ , which acts as an external parameter under which the polarization changes. When θ is adiabatically changed by 2π , the change in polarization, i.e., the shift of the HWF center, is proportional to the Chern number [59, 60]. This is a manifestation of topological pumping [56], with θ being the adiabatic pumping parameter. In our system, the HWF center for a tight-binding chain in Hamiltonian (15) is given by [57]

$$\langle n_x(\theta, k_z) \rangle = \frac{\sum_{i_x} i_x \rho(i_x, \theta, k_z)}{\sum_{i_x} \rho(i_x, \theta, k_z)}, \quad (18)$$

where i_x is the lattice-site index, and $\rho(i_x, \theta, k_z)$ is the density of the HWF and denotes the atomic densities resolved along the x direction as a function of θ and k_z . Here the hybrid density can be written as

$$\rho(i_x, \theta, k_z) = \sum_{\text{occupied states}} |i_x, \theta, k_z\rangle \langle i_x, \theta, k_z|, \quad (19)$$

where $|i_x, \theta, k_z\rangle$ is the hybrid eigenstate of the system. Experimentally, $\rho(i_x, \theta, k_z)$ can be measured by the hybrid time-of-flight images [57], referring to an *in situ* measurement of the density distribution of the atomic cloud in the x direction during free expansion along the z direction for a fixed θ .

We numerically calculate $\langle n_x(\theta, k_z) \rangle$ in a tight-binding chain of length $L_x = 100$ at half-filling (assuming the Fermi energy $E_F = 0$), with the results for typical parameter m_z being shown in Fig. 5. For the case of $m_z = 4$ in Figs. 5(a) and 5(b), the expected critical values between the trivial insulator with $C_{k_z} = 0$ and Chern insulator with $C_{k_z} = -1$ are $k_z = \pm k_z^c = \pm 0.5\pi$. As shown in Fig. 5(a), $\langle n_x(\theta) \rangle$ shows discontinuous jumps of one unit cell within the region $k_z \in (-0.5\pi, 0.5\pi)$, which disappear outside this region. To be more clearly, we plot

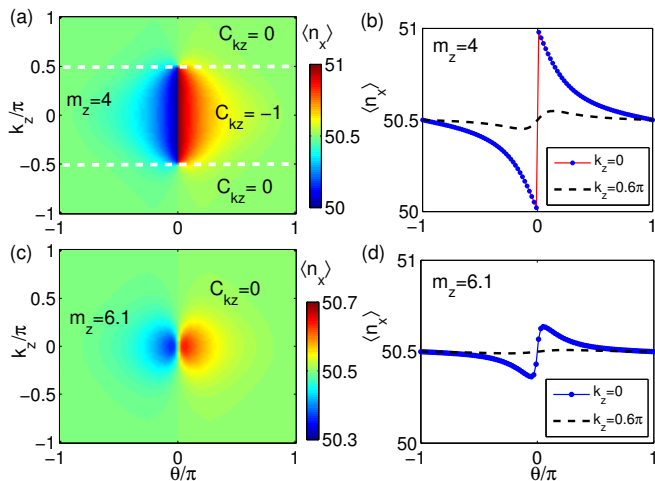


FIG. 5: (Color online) The HWF centers in a tight-binding chain of length $L_x = 100$ at half-filling as a function of the adiabatic pumping parameter θ for different k_z . (a) The profile $\langle n_x(\theta, k_z) \rangle$ for the parameter $m_z = 4$, where $\langle n_x(\theta) \rangle$ (do not) shows a jump of one unit cell for k_z (outside) within the region $(-0.5\pi, 0.5\pi)$, with typical examples shown in (b). (c) The profile for $m_z = 6.1$ shows no jump of $\langle n_x(\theta) \rangle$ for all k_z , with typical examples shown in (d). The corresponding k_z -dependent Chern number C_{k_z} is also plotted both in (a) and (c), with the white dashed lines denoting the critical value between the trivial ($C_{k_z} = 0$) and nontrivial ($C_{k_z} = -1$) cases. Other parameters in (a-d) are $t_0 = 1$ as the energy unit and $t_s = 1$.

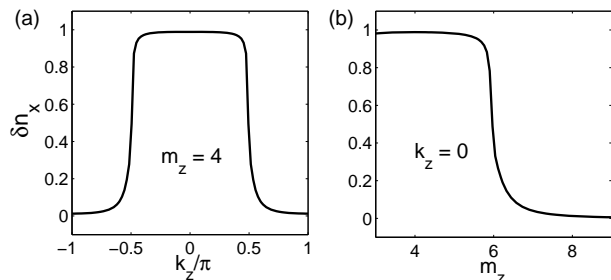


FIG. 6: The maximum variation of the HWF-center shift δn_x . (a) δn_x as a function of k_z for $m_z = 4$. (b) δn_x as a function of m_z for $k_z = 0$. Other parameters in (a) and (b) are $L_x = 100$, $t_0 = 1$ as the energy unit, and $t_s = 1$.

$\langle n_x(\theta) \rangle$ for $k_z = 0$ and $k_z = 0.6\pi$ as two examples in Fig. 5(b). The one-unit-cell jump driven by θ indicates that a single particle is pumped across the system [59, 60], as expected for $C_{k_z} = -1$. The results for $m_z = 6.1$ show no jump of $\langle n_x(\theta) \rangle$ for all k_z in Figs. 5(c) and 5(d), which is consistent with the expected $C_{k_z} = 0$ for $m_z > 6$ in this case. This establishes a direct and clear connection between the shift of the hybrid density center and the topological invariant. Thus one can directly extract the k_z -dependent Chern number from the hybrid time-of-flight images in this cold atom system [57]. The proposed detection method based on topological pumping is not affected by a weak harmonic trap as it does not

require the presence of the sharp edge states [57, 58].

In the HWF-center shifts $\langle n_x(\theta) \rangle$ as shown in Fig. 5, the one-unit jump for topologically nontrivial cases and the continuous variation for trivial cases may be hard to distinct in realistic experiments. It will be more practical to extract the topological invariant from the maximum variation of $\langle n_x(\theta) \rangle$ during adiabatically varying θ

$$\delta n_x \equiv \max\{\langle n_x(\theta) \rangle\} - \min\{\langle n_x(\theta) \rangle\}. \quad (20)$$

In Fig. 6. we numerically calculate δn_x as a function of k_z (m_z) with fixed $m_z = 4$ ($k_z = 0$) for a tight-binding chain. One can find that $\delta n_x \simeq 1$ in the parameter regimes where the system is topologically nontrivial, i.e. $k_z \in (-0.5\pi, 0.5\pi)$ in Fig. 6(a) and $m_z < 6$ in Fig. 6(b), while $\delta n_x \simeq 0$ outside these regimes, corresponding to the trivial cases. Therefore, as long as the system is not close to the critical points, such as $k_z = \pm 0.5\pi$ in Fig. 6(a) and $m_z = 6$ in Fig. 6(b), one can extract the topological invariant in such a measurement as $\delta n_x = |C_{k_z}|$. This simple relationship does not well survive near the topological transition points, where the topological invariant will be more difficult to determine in experiments. It is interesting to note that the proposed measurement of Chern number is straightforward and the quantized pumping approach in the topologically nontrivial (trivial) cases, corresponding to $\delta n_x = 1$ ($\delta n_x = 0$), is robust against weak perturbations under realistic conditions [56, 57].

Finally, we note that the probe of topological edge states in a cold atom system, such as those shown in Fig. 2 and Fig. 3, are also cumbersome. These edge states will generally be washed out by the smooth harmonic potential and thus one may not be able to distinguish them from the bulk states. This problem could be circumvented potentially by using a steep confining potential and imaging the edge states from Bragg signals by means of specifically tuned Raman transitions [61] or from their dynamics after suddenly removing the potential [62]. If the analogous Fermi line states in Fig. 3 can be created, one may further explore the induced topological current in the presence of an additional gauge field acting on the two Weyl points, which is used to break their central symmetry. The simplest example of such a gauge field can be generated by a constant Peierls phase for hopping along the z axis induced by the laser-atom coupling.

V. CONCLUSIONS

In summary, we have proposed an experimental scheme to simulate and explore 3D topological WSMs with cold atoms in a 2D square optical lattice subjected to an artificial dimension from an external cyclical parameter. We have shown that this system is able to describe the essential physics of WSMs with tunable Weyl points, and have investigated the relevant topological properties by calculating the Chern number and the gapless edge states. Furthermore, we have proposed practical methods for

the experimental detection of the mimicked Weyl points and the characteristic topological invariant in this cold atom system. Considering that all the ingredients to implement our scheme in the optical lattice have been achieved in the recent experiments, it is anticipated that the presented proposal will be tested in an experiment in the near future. Our proposed system would provide a promising platform for elaborating the intrinsic exotic physics of WSMs that are elusive in nature.

VI. ACKNOWLEDGEMENTS

We thank T. Mao, Y. X. Zhao, J. Zhang, F. Mei, and Z.-Y. Xue for helpful discussions. This work was

supported by the GRF (Grants No. HKU7045/13P and HKU173051/14P) and the CRF (Grant No. HKU8/11G) of Hong Kong, the SKPBR of China (Grant No. 2011CB922104), the NSFC (Grants No. 11125417 and 11474153), and the PCSIRT (Grant No. IRT1243).

-
- [1] M. Z. Hasan and C. L. Kane, Colloquium: Topological insulators, *Rev. Mod. Phys.* **82**, 3045 (2010).
- [2] X.-L. Qi and S. C. Zhang, Topological insulators and superconductors, *Rev. Mod. Phys.* **83**, 1057 (2011).
- [3] X. Wan, A. M. Turner, A. Vishwannath, and S. Y. Savrasov, Topological semimetal and Fermi-arc surface states in the electronic structure of pyrochlore iridates, *Phys. Rev. B* **83**, 205101 (2011).
- [4] L. Balents, Weyl electrons kiss, *Physics* **4**, 36 (2011).
- [5] A. A. Burkov and L. Balents, Weyl Semimetal in a Topological Insulator Multilayer, *Phys. Rev. Lett.* **107**, 127205 (2011).
- [6] G. Xu, H. Weng, Z. Wang, X. Dai, and Z. Fang, Chern Semimetal and the Quantized Anomalous Hall Effect in HgCr_2Se_4 , *Phys. Rev. Lett.* **107**, 186806 (2011).
- [7] P. Delplace, J. Li, and D. Carpentier, Topological Weyl semi-metal from a lattice model, *Europhys. Lett.* **97**, 67004 (2012).
- [8] Y. X. Zhao and Z. D. Wang, Disordered Weyl semimetals and their topological family, *Phys. Rev. Lett.* **114**, 206602 (2015).
- [9] G. E. Volovik, *The Universe in a Helium Droplet* (Clarendon, Oxford, 2003).
- [10] Y. X. Zhao and Z. D. Wang, Topological Classification and Stability of Fermi Surfaces, *Phys. Rev. Lett.* **110**, 240404 (2013).
- [11] A. A. Zyuzin and A. A. Burkov, Topological response in Weyl semimetals and the chiral anomaly, *Phys. Rev. B* **86**, 115133 (2012); Z. Wang and S.-C. Zhang, Chiral anomaly, charge density waves, and axion strings from Weyl semimetals, *Phys. Rev. B* **87**, 161107 (2013).
- [12] S. A. Parameswaran, T. Grover, D. A. Abanin, D. A. Pesin, and A. Vishwanath, Probing the Chiral Anomaly with Nonlocal Transport in Three-Dimensional Topological Semimetals, *Phys. Rev. X* **4**, 031035 (2014).
- [13] S.-Y. Xu, C. Liu, S. K. Kushwaha, R. Sankar, J. W. Krizan, I. Belopolski, M. Neupane, G. Bian, N. Alidoust, T.-R. Chang, H.-T. Jeng, C.-Y. Huang, W.-F. Tsai, H. Lin, P. P. Shibayev, F.-C. Chou, R. J. Cava, and M. Z. Hasan, Observation of Fermi arc surface states in a topological metal, *Science* **347**, 294 (2015).
- [14] S.-M. Huan, I. Belopolski, C.-C. Lee, G. Chang, B. Wang, N. Alidoust, G. Bian, M. Neupane, A. Bansil, H. Lin, and M. Z. Hasan, An inversion breaking Weyl semimetal state in the TaAs material class, arXiv:1501.00755; S.-M. Huan, S.-Y. Xu, I. Belopolski, C.-C. Lee, G. Chang, B. Wang, N. Alidoust, M. Neupane, H. Zheng, D. Sanchez, A. Bansil, G. Bian, H. Lin, and M. Z. Hasan, A new type of Weyl semimetal with quadratic double Weyl fermions in SrSi_2 , arXiv:1503.05868.
- [15] B. Q. Lv, H. M. Weng, B. B. Fu, X. P. Wang, H. Miao, J. Ma, P. Richard, X. C. Huang, L. X. Zhao, G. F. Chen, Z. Fang, X. Dai, T. Qian, and H. Ding, Discovery of Weyl semimetal TaAs, arXiv:1502.04684; B. Q. Lv, N. Xu, H. M. Weng, J. Z. Ma, P. Richard, X. C. Huang, L. X. Zhao, G. F. Chen, C. Matt, F. Bisti, V. Stokov, J. Mesot, Z. Fang, X. Dai, T. Qian, M. Shi, and H. Ding, Observation of Weyl nodes in TaAs, arXiv:1503.09188.
- [16] S.-Y. Xu, I. Belopolski, N. Alidoust, M. Neupane, C. Zhang, R. Sankar, S.-M. Huang, C.-C. Lee, G. Chang, B. Wang, G. Bian, H. Zheng, D. S. Sanchez, F. Chou, H. Lin, S. Jia, and M. Z. Hasan, Experimental realization of a topological Weyl semimetal phase with Fermi arc surface states in TaAs, arXiv:1502.03807.
- [17] C. Zhang, S.-Y. Xu, I. Belopolski, Z. Yuan, Z. Lin, B. Tong, N. Alidoust, C.-C. Lee, S.-M. Huang, H. Lin, M. Neupane, D. S. Sanchez, H. Zheng, G. Bian, J. Wang, C. Zhang, T. Neupert, M. Z. Hasan, and S. Jia, Observation of the Adler-Bell-Jackiw chiral anomaly in a Weyl semimetal, arXiv:1503.02630.
- [18] L. Lu, L. Fu, J. D. Joannopoulos, and M. Soljačić, Weyl points and line nodes in gyroid photonic crystals, *Nat. Photonics* **7**, 294 (2013).
- [19] L. Lu, Z. Wang, D. Ye, L. Ran, L. Fu, J. D. Joannopoulos, and M. Soljačić, Experimental observation of Weyl points, arXiv:1502.03438.
- [20] M. Lewenstein, A. Sanpera, V. Ahufinger, B. Damski, A. S. De, and U. Sen, Ultracold atomic gases in optical lattices: mimicking condensed matter physics and beyond, *Adv. Phys.* **56**, 243 (2007).
- [21] D.-W. Zhang, Z. D. Wang, and S.-L. Zhu, Relativistic quantum effects of Dirac particles simulated by ultracold atoms, *Front. Phys.* **7**, 31 (2012); E. Alba, X. Fernandez-Gonzalvo, J. Mur-Petit, J. J. Garcia-Ripoll, and J. K. Pachos, Simulating Dirac fermions with Abelian and non-Abelian gauge fields in optical lattices, *Ann. Phys.* **328**,

- 64 (2013).
- [22] Y.-J. Lin, R. L. Compton, K. Jiménez-García, J. V. Porto, and I. B. Spielman, Synthetic magnetic fields for ultracold neutral atoms, *Nature (London)* **462**, 628 (2009).
- [23] Y.-J. Lin, K. Jiménez-García, and I. B. Spielman, A spin-orbit coupled Bose-Einstein condensate, *Nature (London)* **471**, 83 (2011).
- [24] P. Wang, Z.-Q. Yu, Z. Fu, J. Miao, L. Huang, S. Chai, H. Zhai, and J. Zhang, Spin-Orbit Coupled Degenerate Fermi Gases, *Phys. Rev. Lett.* **109**, 095301 (2012).
- [25] L. W. Cheuk, A. T. Sommer, Z. Hadzibabic, T. Yefsah, W. S. Bakr, and M. W. Zwierlein, Spin-Injection Spectroscopy of a Spin-Orbit Coupled Fermi Gas, *Phys. Rev. Lett.* **109**, 095302 (2012).
- [26] See the reviews, J. Dalibard, F. Gerbier, G. Juzeliūnas, and P. Öhberg, Colloquium: Artificial gauge potentials for neutral atoms, *Rev. Mod. Phys.* **83**, 1523 (2011); V. Galitski and I. B. Spielman, Spin-orbit coupling in quantum gases, *Nature (London)* **494**, 49 (2013); X. Zhou, Y. Li, Z. Cai, and C. Wu, Unconventional states of bosons with synthetic spin-orbit coupling, *J. Phys. B: At. Mol. Opt. Phys.* **46**, 134001 (2013); N. Goldman, G. Juzeliūnas, P. Öhberg, and I. B. Spielman, Light-induced gauge fields for ultracold atoms, *Rep. Prog. Phys.* **77**, 126401 (2014); H. Zhai, Degenerate quantum gases with spinOrbit coupling: a review, *Rep. Prog. Phys.* **78**, 026001 (2015).
- [27] L.-B. Shao, S.-L. Zhu, L. Sheng, D. Y. Xing, and Z. D. Wang, Realizing and detecting the quantum Hall effect without Landau levels by using ultracold atoms, *Phys. Rev. Lett.* **101**, 246810 (2008); X.-J. Liu, X. Liu, C. Wu, and J. Sinova, Quantum anomalous Hall effect with cold atoms trapped in a square lattice, *Phys. Rev. A* **81**, 033622 (2010).
- [28] N. Goldman, I. Satija, P. Nikolic, A. Bermudez, M. A. Martin-Delgado, M. Lewenstein, and I. B. Spielman, Realistic time-reversal invariant topological insulators with neutral atoms, *Phys. Rev. Lett.* **105**, 255302 (2010).
- [29] B. Béri and N. R. Cooper, \mathbb{Z}_2 topological insulators in ultracold atomic gases, *Phys. Rev. Lett.* **107**, 145301 (2011).
- [30] E. Alba, X. Fernandez-Gonzalvo, J. Mur-Petit, J. K. Pachos, and J. J. García-Ripoll, Seeing topological order in time-of-flight measurements, *Phys. Rev. Lett.* **107**, 235301 (2011).
- [31] C. Zhang, S. Tewari, R. M. Lutchyn, and S. Das Sarm, $p_x + ip_y$ superfluid from s-wave interactions of fermionic cold atoms, *Phys. Rev. Lett.* **101**, 160401 (2008); S.-L. Zhu, L.-B. Shao, Z. D. Wang, and L.-M. Duan, Probing non-Abelian statistics of Majorana fermions in ultracold atomic superfluid, *Phys. Rev. Lett.* **106**, 100404 (2011); X.-J. Liu, K. T. Law, and T. K. Ng, Realization of 2D spin-orbit interaction and exotic topological orders in cold atoms, *Phys. Rev. Lett.* **112**, 086401 (2014).
- [32] K. Sun, W. V. Liu, A. Hemmerich, and S. Das Sarma, Topological semimetal in a fermionic optical lattice, *Nat. Phys* **8**, 67 (2012).
- [33] H. M. Price and N. R. Cooper, Mapping the Berry curvature from semiclassical dynamics in optical lattices, *Phys. Rev. A* **85**, 033620 (2012).
- [34] X.-J. Liu, K. T. Law, T. K. Ng, and P. A. Lee, Detecting topological phases in cold atoms, *Phys. Rev. Lett.* **111**, 120402 (2013).
- [35] D. A. Abanin, T. Kitagawa, I. Bloch, and E. Demler, Interferometric approach to measuring band topology in 2D optical lattices, *Phys. Rev. Lett.* **110**, 165304 (2013).
- [36] D.-L. Deng, S.-T. Wang, and L.-M. Duan, Direct probe of topological order for cold atoms, *Phys. Rev. A* **90**, 041601(R) (2104).
- [37] A. Bermudez, L. Mazza, M. Rizzi, N. Goldman, M. Lewenstein, and M. A. Martin-Delgado, Wilson fermions and axion electrodynamics in optical lattices, *Phys. Rev. Lett.* **105**, 190404 (2010).
- [38] S.-T. Wang, D.-L. Deng, and L.-M. Duan, Probe of three-dimensional chiral topological insulators in an optical lattice, *Phys. Rev. Lett.* **113**, 033002 (2014).
- [39] M. Atala, M. Aidelsburger, J. T. Barreiro, D. Abanin, T. Kitagawa, E. Demler, and I. Bloch, Direct measurement of the Zak phase in topological Bloch bands, *Nat. Phys.* **9**, 795 (2013).
- [40] G. Jotzu, M. Messer, R. Desbuquois, M. Lebrat, T. Uehlinger, D. Greif, and T. Esslinger, Experimental realisation of the topological Haldane model with ultracold fermions, *Nature (London)* **515**, 237 (2014).
- [41] M. Aidelsburger, M. Lohse, C. Schweizer, M. Atala, J. T. Barreiro, S. Nascimbène, N. R. Cooper, I. Bloch, and N. Goldman, Measuring the Chern number of Hofstadter bands with ultracold bosonic atoms, *Nat. Phys.* **11**, 162 (2015).
- [42] Y. E. Kraus, Y. Lahini, Z. Ringel, M. Verbin, and O. Zilberber, Topological states and adiabatic pumping in quasicrystals, *Phys. Rev. Lett.* **109**, 106402 (2012); M. Verbin, O. Zilberberg, Y. E. Kraus, Y. Lahini, and Y. Silberberg, Observation of topological phase transitions in photonic quasicrystals, *Phys. Rev. Lett.* **110**, 076403 (2013).
- [43] L.-J. Lang, X. Cai, and S. Chen, Edge states and topological phases in one-dimensional optical superlattices, *Phys. Rev. Lett.* **108**, 220401 (2012).
- [44] F. Mei, S.-L. Zhu, Z.-M. Zhang, C. H. Oh, and N. Goldman, Simulating \mathbb{Z}_2 topological insulators with cold atoms in a one-dimensional optical lattice, *Phys. Rev. A* **85**, 013638 (2012); S.-L. Zhu, Z.-D. Wang, Y.-H. Chan, and L.-M. Duan, Topological Bose-Mott insulators in a one-dimensional optical superlattice, *Phys. Rev. Lett.* **110**, 075303 (2013).
- [45] A. Celi, P. Massignan, J. Ruseckas, N. Goldman, I. B. Spielman, G. Juzeliūnas, and M. Lewenstein, Synthetic gauge fields in synthetic dimensions, *Phys. Rev. Lett.* **112**, 043001 (2014); O. Boada, A. Celi, J. I. Latorre, and M. Lewenstein, Quantum simulation of an extra dimension, *Phys. Rev. Lett.* **108**, 133001 (2012).
- [46] B. K. Stuhl, H.-I Lu, L. M. Ayccock, D. Genkina, and I. B. Spielman, Visualizing edge states with an atomic Bose gas in the quantum Hall regime, arXiv:1502.02496; M. Mancini, G. Pagano, G. Cappellini, L. Livi, M. Rider, J. Catani, C. Sias, P. Zoller, M. Inguscio, M. Dalmonte, and L. Fallani, Observation of chiral edge states with neutral fermions in synthetic Hall ribbons, arXiv:1502.02495.
- [47] J. H. Jiang, Tunable topological Weyl semimetal from simple-cubic lattices with staggered fluxes, *Phys. Rev. A* **85**, 033640 (2012).
- [48] T. Dubcek, C. J. Kennedy, L. Lu, W. Ketterle, M. Soljacic and H. Buljan, Weyl points in three-dimensional optical lattices: synthetic magnetic monopoles in momentum space, arXiv:1412.7615.

- [49] W.-Y. He, S. Zhang, and K. T. Law, The realization and detection of Weyl semimetals in cold atomic systems, arXiv:1501.02348.
- [50] S. Ganeshan and S. Das Sarma, Constructing a Weyl semimetal by stacking one-dimensional topological phases, *Phys. Rev. B* **91**, 125438 (2015)
- [51] P. Schauß, J. Zeiher, T. Fukuhara, S. Hild, M. Cheneau, T. Macrì, T. Pohl, I. Bloch, C. Gross, Crystallization in Ising quantum magnets, *Science* **347**, 1455 (2015).
- [52] Y. X. Zhao and Z. D. Wang, Topological connection between the stability of Fermi surfaces and topological insulators and superconductors, *Phys. Rev. B* **89**, 075111 (2014); Y. X. Zhao and Z. D. Wang, Exotic topological types of Majorana zero modes and their universal quantum manipulation, *Phys. Rev. B* **90**, 115158 (2014).
- [53] L. Tarruell, D. Greif, T. Uehlinger, G. Jotzu, and T. Esslinger, Creating, moving and merging Dirac points with a Fermi gas in a tunable honeycomb lattice, *Nature (London)* **483**, 302 (2012); T. Uehlinger, D. Greif, G. Jotzu, L. Tarruell, T. Esslinger, L. Wang, and M. Troyer, Double transfer through Dirac points in a tunable honeycomb optical lattice, *Eur. Phys. J. Special Topics* **217**, 121(2013).
- [54] L.-K. Lim, J.-N. Fuchs, and G. Montambaux, Bloch-Zener oscillations across a merging transition of Dirac points, *Phys. Rev. Lett.* **108**, 175303 (2012).
- [55] L. Duca, T. Li, M. Reitter, I. Bloch, M. Schleier-Smith, and U. Schneider, An Aharonov-Bohm interferometer for determining Bloch band topology, *Science* **347**, 288 (2015)
- [56] D. J. Thouless, Quantization of particle transport, *Phys. Rev. B* **27**, 6083 (1983); Q. Niu, Towards a quantum pump of electric charges, *Phys. Rev. Lett.* **64**, 1812 (1990).
- [57] L. Wang, A. A. Soluyanov, and M. Troyer, Proposal for direct measurement of topological invariants in optical lattices, *Phys. Rev. Lett.* **110**, 166802 (2013); L. Wang, M. Troyer, and X. Dai, Topological charge pumping in a one-dimensional optical lattice, *Phys. Rev. Lett.* **111**, 026802 (2013).
- [58] F. Mei, J.-B You, D.-W Zhang, X.-C. Yang, R. Fazio, S.-L Zhu, and L. C. Kwek, Topological insulator and particle pumping in a one-dimensional shaken optical lattice, *Phys. Rev. A* **90**, 063638 (2014); D.-W. Zhang, F. Mei, Z.-Y. Xue, S.-L. Zhu, and Z. D. Wang, Simulation and measurement of the fractional particle number in one-dimensional optical lattices, arXiv:1502.00059; R. Wei and E. J. Mueller, Anomalous charge pumping in a one-dimensional optical superlattice, arXiv:1502.04208.
- [59] N. Marzari, A. Mostofi, J. R. Yates, I. Souza, and D. Vanderbilt, Maximally localized Wannier functions: Theory and applications, *Rev. Mod. Phys.* **84**, 1419 (2012).
- [60] R. D. King-Smith and D. Vanderbilt, Theory of polarization of crystalline solids, *Phys. Rev. B* **47**, 1651 (1993); S. Coh and D. Vanderbilt, Electric polarization in a Chern insulator, *Phys. Rev. Lett.* **101**, 107603 (2009).
- [61] N. Goldman, J. Beugnon, and F. Gerbier, Detecting chiral edge states in the Hofstadter optical lattice, *Phys. Rev. Lett.* **108**, 255303 (2012); M. Buchhold, D. Cocks, and W. Hofstetter, Effects of smooth boundaries on topological edge modes in optical lattices, *Phys. Rev. A* **85**, 063614 (2012).
- [62] N. Goldman, J. Dalibard, A. Dauphin, F. Gerbier, M. Lewenstein, P. Zoller, and I. B. Spielman, Direct imaging of topological edge states in cold-atom systems, *Proc. Natl. Acad. Sci. USA* **110**, 6736 (2013).